Numerical investigations of flow and energy fields near a thermoacoustic couple

Haruko Ishikawa and David J. Mee
Department of Mechanical Engineering, The University of Queensland, St. Lucia, Queensland 4072, Australia

(Received 19 January 2001; revised 9 September 2001; accepted 23 October 2001)

The flow field and the energy transport near thermoacoustic couples are simulated using a 2D full Navier–Stokes solver. The thermoacoustic couple plate is maintained at a constant temperature; plate lengths, which are ''short'' and ''long'' compared with the particle displacement lengths of the acoustic standing waves, are tested. Also investigated are the effects of plate spacing and the amplitude of the standing wave. Results are examined in the form of energy vectors, particle paths, and overall entropy generation rates. These show that a net heat-pumping effect appears only near the edges of thermoacoustic couple plates, within about a particle displacement distance from the ends. A heat-pumping effect can be seen even on the shortest plates tested when the plate spacing exceeds the thermal penetration depth. It is observed that energy dissipation near the plate increases quadratically as the plate spacing is reduced. The results also indicate that there may be a larger scale vortical motion outside the plates which disappears as the plate spacing is reduced. [DOI: 10.1121/1.1430687]

PACS numbers: 43.35.Ud [SGK]

I. INTRODUCTION

Thermoacoustic engines are devices which make use of thermoacoustic phenomena and function as heat pumps or prime movers. They can provide cooling or heating using environmentally benign gases. Despite recent developments in thermoacoustic engines (Swift, 1999), there are many areas requiring further investigation in order to better predict their performance and guide future designs of thermoacoustic engines. Particularly lacking is overall research into heat exchangers in thermoacoustic engines, for which there are no established design methodologies.

Analytical models of thermoacoustic devices have been developed for the calculation of time-averaged energy fluxes for devices operating at low pressure amplitudes (Swift, 1988). However, these models do not account for entrance effects at the ends of regenerators and heat exchangers. The main differences between regenerators and heat exchangers are that regenerator plates are normally at least ten times as long as heat exchanger plates and have a temperature gradient along their length. Heat exchanger plates are usually considered to be isothermal and short enough that plate end effects should prevail over their length.

The motivation for the current work is to understand the energy transfer mechanisms at heat exchangers in thermoacoustic devices. However, in order to model the heat exchanger section only, boundary conditions reproducing the energy and flow fields developed due to the interaction between the regenerator and the heat exchanger must be applied at the edge of the domain. Suitable information to apply at such a boundary is currently not available.

Therefore, the current work deals with the simpler case of a thermoacoustic couple. The thermoacoustic couple retains most of the physical processes that occur in heat exchangers but is more tractable numerically. The thermoacoustic couple was originally proposed and tested by Wheatley *et al.* (1983) in order to clearly demonstrate the thermoacoustic phenomenon. The thermoacoustic couple is a stack of a few short plates in a resonator and is designed so that the stack can be placed at any position within the standing wave.

Several works have addressed the numerical simulation of thermoacoustic devices, but most have concentrated on the regenerators [Worlikar and Knio (1996); Watanabe *et al.* (1997); Yuan *et al.* (1997)]. In addition, although nonlinearity is incorporated into their models, various simplifications to the governing equations have been made.

The work of Cao *et al.* (1996) is the only one that simulates isothermal plates in a standing wave using the full 2D Navier–Stokes equations. However, only one plate length (which corresponds to the length of typical regenerator plates) was tested and the simulation became unstable for small plate spacings.

An analytical model for heat exchanger plates near a stack is presented by Mozurkewich (1998a). Worlikar and Knio (1999) included heat exchanger plates in their simulation. They considered a single plate but imposed isothermal conditions at either edge to represent hot and cold heat exchangers. In order to simplify the governing equations, assumptions such as low Mach number and constant viscosity and thermal conductivity were made. Their simulations indicate that there is heat pumping action on heat exchanger plates that are as short as the particle displacement length and that the efficiency of a thermoacoustic engine is optimum when the heat exchanger plates are approximately that length. However, the effect of plate spacing was not tested in their work.

II. DOMAIN AND OPERATING CONDITIONS

Figure 1(a) is a slice (in the $x-y$ plane) of a thermoacoustic couple. The extent of the simulation domain is indi-

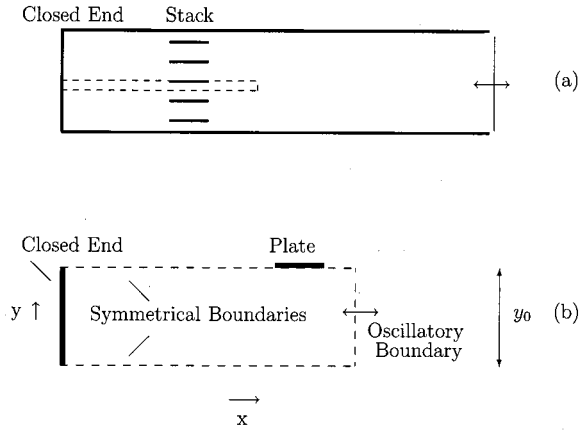

FIG. 1. (a) Thermoacoustic couple in a resonator. (b) The computational domain.

cated by the dotted lines and is enlarged in Fig. 1(b). The simulation model is an isothermal plate subject to a standing wave in a helium-filled resonator. The plate thickness is not modeled. y_0 is the plate half-spacing. Throughout this paper the right-hand end of the plate in Fig. 1(b) is referred to as the outer edge and the left end is referred to as the inner edge.

The mean temperature, T_m, is 300 K, the mean pressure, p_m, is 10 kPa, the frequency, f, is 100 Hz, and the outer edge of the plate is located one-eighth of the wavelength, 126 cm, from the closed end of the resonator. The oscillatory boundary conditions are specified 0.0085λ from the outer edge of the plate where λ is the wavelength. These operating conditions were chosen to replicate the test cases of Cao *et al.* (1996). The mean pressure used by Cao *et al.* (1996) is approximately one-tenth of atmospheric pressure (assuming T_m and f to be 300 K and 100 Hz, respectively). This is two orders of magnitude smaller than that commonly used for existing operating thermoacoustic devices. Parametric studies for operating conditions closer to those of existing thermoacoustic devices were done by Ishikawa (2000). The characteristics of the flow and energy fields for the various plate geometries were similar to those tested at the operating conditions of Cao *et al.* despite the fact that the Reynolds numbers differed by two orders of magnitude.

Table I presents conditions for the present test cases. L is the plate length. $\delta_{km}(=\sqrt{2k/\omega})$ is the thermal penetration depth where k is the thermal diffusivity and ω is the angular frequency. δ_{km} is 0.24 cm when evaluated at T_m and p_m.

Turbulence is neglected for all test cases because the critical Reynolds number, $\mathrm{Re}=2u_1/\sqrt{(\nu\omega)}$, as defined by Merkli and Thomann (1975), was always below 400.

Mach numbers, M, are evaluated at the mean temperature and are based on the velocity amplitude at the velocity antinode of the standing wave. P_A/p_m is the drive ratio, which is the ratio of pressure amplitude at the pressure antinode of the standing wave, P_A, and the mean pressure. Δx and Δy are the grid sizes in the x and y directions. The particle displacement length, $2u_1/\omega$ (where u_1 is the first-order x-component velocity amplitude) evaluated at the plate outer edge, is 2.3 cm when the Mach number is 0.01.

The sizes of the spatial and temporal grids used are close to those of Cao *et al.* (1996). Grid independency was confirmed by comparing the energy flux at the plate surface for grids of various sizes in Ishikawa (2000). As shown in Sec. VII, the results the current work agree with those of Cao *et al.* which, in turn agree with the analytical calculations of Mozurkewich (1998b).

TABLE I. Thermoacoustic couple test cases. The test gas is helium, $\gamma=5/3$, Pr=0.68, $p_m=1.0$ kPa. $2u_1/\omega=2.3$ cm, $\delta_{km}=0.24$ cm.

Run	L	δ_{km}/y_0	M	$P_A/p_m[\%]$	$\Delta x/\lambda$	$\Delta y/\delta_{km}$
1	$22u_1/\omega$	0.3	0.03	5.1	$2.5E-4$	$8.3E-2$
2	$22u_1/\omega$	0.6	0.03	5.1	$2.5E-4$	$4.2E-2$
3	$22u_1/\omega$	1.0	0.03	5.1	$2.5E-4$	$4.2E-2$
4	$22u_1/\omega$	1.2	0.03	5.1	$2.5E-4$	$4.2E-2$
5	$22u_1/\omega$	1.6	0.03	5.1	$2.5E-4$	$4.2E-2$
6	$22u_1/\omega$	1.8	0.03	5.1	$2.5E-4$	$4.2E-2$
7	$22u_1/\omega$	0.3	0.01	1.7	$2.5E-4$	$8.3E-2$
8	$22u_1/\omega$	0.3	0.02	3.4	$2.5E-4$	$8.3E-2$
9	$22u_1/\omega$	0.3	0.04	6.8	$2.5E-4$	$8.3E-2$
10	$22u_1/\omega$	0.3	0.05	8.5	$2.5E-4$	$8.3E-2$
11	$2u_1/\omega$	0.3	0.01	1.7	$8.2E-5$	$8.3E-2$
12	$2u_1/\omega$	2.0	0.01	1.7	$8.2E-5$	$4.2E-2$
13	$2u_1/\omega$	3.0	0.01	1.7	$8.2E-5$	$2.8E-2$
14	u_1/ω	0.3	0.01	1.7	$8.2E-5$	$8.3E-2$
15	u_1/ω	2.0	0.01	1.7	$8.2E-5$	$4.2E-2$
16	u_1/ω	3.0	0.01	1.7	$8.2E-5$	$2.8E-2$

III. NUMERICAL METHOD

The continuity, momentum, and energy equations for a 2D compressible ideal gas at low Mach number are solved in the current simulations. The commercial code PHOENICS, developed by CHAM Ltd., which solves the governing equations using a finite volume method (Spalding, 1991), was used for the present simulations. Schemes used to discretize the governing equations in PHOENICS give second-order accuracy in space and first-order accuracy in time. In order to couple the momentum and continuity equations, PHOENICS uses the SIMPLEST (SIMPLE ShorTend) algorithm suggested by Spalding (1980), which is a variant of the SIMPLE (semi-implicit method for pressure-linked equations) method (Patankar and Spalding, 1972).

In the current work, convergence of the simulation was determined by monitoring the change in each variable after each iteration and also by looking at the energy balance of the simulation domain. Simulations were considered to have reached steady state when the changes in all quantities were less than 0.1% of their fluctuating amplitudes from one cycle to the next. At this stage, the difference between the cycle-averaged heat flux through the plate and the energy flux through the oscillatory boundary was less than 5% of the maximum fluctuating energy flux in the domain. Larger energy imbalances are attributed to the fact that the energy flux and heat flux are second-order quantities which are derived from differences between two first-order quantities. Limitations of the code (such as single precision in calculations) restricted the overall accuracy that could be achieved in the second-order quantities.

In order to close the equation set, auxiliary equations for thermodynamic properties, transport properties, and bound-

ary conditions are required. In the current work, the gas used for the simulations is helium. The equation of state for an ideal gas is used to calculate the density. PHOENICS solves the energy equation in terms of enthalpy assuming a calorically perfect gas. The transport properties required in the current model are the viscosity and the thermal conductivity of the gas. For simplicity, a power-law model is used for the variation of viscosity with temperature

$$\mu = \mu' \left(\frac{T}{T'} \right)^s, \tag{1}$$

where s is a constant, and μ' is the dynamic viscosity at the reference temperature T'. The constant s used for the current work is 0.647, which is appropriate for temperatures between 15 and 460 K (Chapman and Cowling, 1970). In the current work, T' was chosen as the initial mean temperature of the whole simulation domain.

The kinematic viscosity is calculated by dividing Eq. (1) by the temperature-dependent density of the gas. The Prandtl number is assumed to be constant over the temperature range of the simulations. This, along with the assumption of constant specific heats, leads to the variation of thermal conductivity with temperature having the same form as Eq. (1) with the same exponent.

IV. INITIAL AND BOUNDARY CONDITIONS

At the start of the simulations all variables throughout the simulation domain were set at their mean values as follows:

$$\left.\begin{aligned} u &= 0 \\ v &= 0 \\ T &= T_m \end{aligned}\right\} \quad \text{at } t=0 \quad \text{at all } x\text{- and } y\text{-cells}, \tag{2}$$

where u and v are the x- and y-components of the velocity vector and T_m is the mean temperature of the gas.

The conditions imposed on each boundary [except for the oscillatory boundary of Fig. 1(b), hereafter referred to as BC_{os}], are as follows:

$$\left.\begin{aligned} u &= 0 \\ v &= 0 \\ \frac{dT}{dx} &= 0 \end{aligned}\right\} \quad \text{Closed end}, \tag{3}$$

$$\left.\begin{aligned} v &= 0 \\ \frac{dT}{dy} &= 0 \end{aligned}\right\} \quad \text{Symmetrical boundary}, \tag{4}$$

$$\left.\begin{aligned} u &= 0 \\ v &= 0 \\ T &= T_m \end{aligned}\right\} \quad \text{Plate}. \tag{5}$$

Special considerations were required at the oscillatory boundary, BC_{os}. In the current work, thermoacoustic couples were simulated by applying standing-wave conditions at the open end of the simulation domain [BC_{os} of Fig. 1(b)]. It is apparent that the flow field near the plate is strongly y dependent, and it would not be appropriate to use standing-wave conditions if the oscillatory boundary was placed very near the plate. In order to take account of the plate end effect, Cao *et al.* (1996) varied the temporal phase shift between the pressure and the velocity from that of a standing wave at oscillatory boundaries on either side of the plates. Their simulation domain is similar to the current work except that it does not extend to the tube wall; instead, it encompasses just the region near the plate. In the current work, one end of the simulation domain is chosen as the closed end of the tube. At the other end, an oscillatory boundary condition (an ideal standing-wave condition) is specified far enough away from the plate that moving the boundary further away did not significantly affect the simulation results presented in this paper.

Since a constant temperature is specified at the plate, a rise in the mean temperature of the gas in the simulation domain, due to viscous dissipation, will cause heat to flow out of the domain through the plate. In order to maintain an energy balance for the simulation domain, any heat entering (or leaving) the plate must be balanced by an energy flux through the oscillatory boundary. The values of p, u, and T at BC_{os} are set to be those of a standing wave. However, gradients in properties are not fixed here and energy flux can pass through the oscillatory boundary because of these gradients. The oscillatory boundary is further discussed in Sec. VII.

The pressure, the velocity, and the temperature at BC_{os} are as follows:

$$p = p_m + \mathrm{Re}\{p_1 e^{i\omega t}\}, \tag{6}$$

$$u = \mathrm{Re}\{u_1 e^{i\omega t}\}, \tag{7}$$

$$T = T_m + \mathrm{Re}\{T_1 e^{i\omega t}\}, \tag{8}$$

where Re{ } signifies the real part and p_1, u_1, and T_1 are the first-order complex amplitudes of pressure, x component of velocity and temperature, respectively, fluctuating about their mean values. p_1, u_1, and T_1 for an ideal standing wave are

$$p_1 = P_A \cos(kx), \quad u_1 = i \frac{-P_A}{\rho_m a} \sin(kx), \tag{9}$$

and

$$T_1 = p_1 / \rho_m c_p,$$

where a is the sound speed, k is the wave number, ρ_m is the mean density, and c_p is the specific heat at a constant pressure.

V. VISUALIZATION OF THE ENERGY AND FLOW FIELDS

In order to visualize the direction of heat flux, temperature contours generally are sufficient for steady heat transfer problems but they are not suitable when convection is involved. For the latter case, the energy density flux (as displayed by Cao *et al.*, 1996) is useful for visualizing energy transfer. The x- and y-components of energy flux density can be written as

$$\dot{e}_x = \rho u \left(\frac{1}{2} v^2 + h \right) - K \frac{\partial T}{\partial x} - (u \sigma_{xx} + v \sigma_{yx}), \tag{10}$$

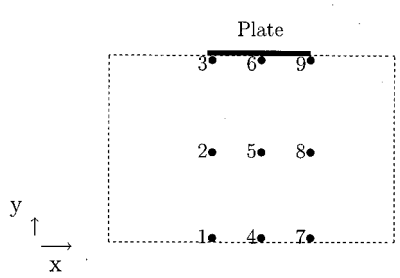

FIG. 2. Starting positions for nine particles in the simulation domain.

where v is the total velocity, h is the enthalpy, σ_{ij} signifies components of the viscous stress tensor, K is the thermal conductivity, and

$$\dot{e}_y = \rho v\left(\frac{1}{2}v^2 + h\right) - K\frac{\partial T}{\partial y} - (u\sigma_{xy} + v\sigma_{yy}), \tag{11}$$

where

$$\sigma_{xx} = \mu\frac{2}{3}\left[2\frac{\partial u}{\partial x} - \frac{\partial v}{\partial y}\right], \quad \sigma_{yy} = \mu\frac{2}{3}\left[2\frac{\partial v}{\partial y} - \frac{\partial u}{\partial x}\right],$$
$$\sigma_{xy} = \mu\left[\frac{\partial u}{\partial y} + \frac{\partial v}{\partial x}\right] = \sigma_{yx}. \tag{12}$$

While energy vectors are useful for visualizing the energy field, particle traces are useful for visualizing the flow field. The movements of gas parcels were traced over several cycles. The initial locations of nine particles are shown in Fig. 2. The initial x locations are at each end and at the middle of the plate. The initial y locations are one cell above the plate surface, at a quarter of the interplate spacing, and near the middle of the interspacing.

The locations of the particles after a short time increment Δt are calculated by multiplying velocities (in both x- and y directions) at the initial particle location by the time-step size Δt. Then, velocities at the new locations are used to calculate the particle locations at time, $2\times\Delta t$. This process is repeated every time step until the end of the cycle. Particles are traced for a maximum of three consecutive cycles after the simulations are considered to have reached steady state.

In order to estimate the sensitivity of the particle traces to time-step size, particle tracks were calculated for two different time-step sizes $\Delta t = 0.28\%$ and 0.21% of the duration of a cycle. The differences between locations at the start and end of a cycle for the two different time-step sizes were less than 0.1% of the half-plate spacing y_0.

VI. CALCULATION OF ENERGY DISSIPATION

As described by Landau (1959), energy dissipation in the simulation domain can be calculated from

$$\dot{e}_{\text{diss}} = -T_0\dot{s}_{\text{gen}}, \tag{13}$$

where $\dot{s}_{\text{gen}}$ is the entropy generation rate per unit volume, and T_0 is the temperature that the system would have if it were in thermodynamic equilibrium at that entropy. The entropy generation rate per unit volume in an ideal gas with viscosity for a two-dimensional system in Cartesian coordinates is

$$\dot{s}_{\text{gen}} = \frac{K}{T^2}\left[\left(\frac{\partial T}{\partial x}\right)^2 + \left(\frac{\partial T}{\partial y}\right)^2\right] + \frac{\mu}{T}\left\{-\frac{2}{3}\left(\frac{\partial u}{\partial x} + \frac{\partial v}{\partial y}\right)^2 + 2\left(\frac{\partial u}{\partial x}\right)^2 + 2\left(\frac{\partial v}{\partial y}\right)^2 + \left(\frac{\partial v}{\partial x} + \frac{\partial u}{\partial y}\right)^2\right\}, \tag{14}$$

where T is the mean temperature of the small control volume. [See, for example, Bird *et al.* (1960) or Bejan (1982) for a derivation of Eq. (14).]

Energy dissipation at the plate surface can be calculated from

$$\dot{e}_{\text{diss}} = \frac{1}{4}\frac{(p_1)^2}{\rho_m a^2}\delta_\kappa\frac{\gamma-1}{1+\epsilon_s}\omega + \frac{1}{4}\rho_m(u_1)^2\delta_\nu\omega, \tag{15}$$

where γ is the specific heat ratio and δ_ν is the viscous penetration depth $(=\sqrt{2\nu/\omega})$. This analytical expression was derived by Swift (1988) for the short engine model with a boundary layer approximation $(y_0 \gg \delta_\kappa)$.

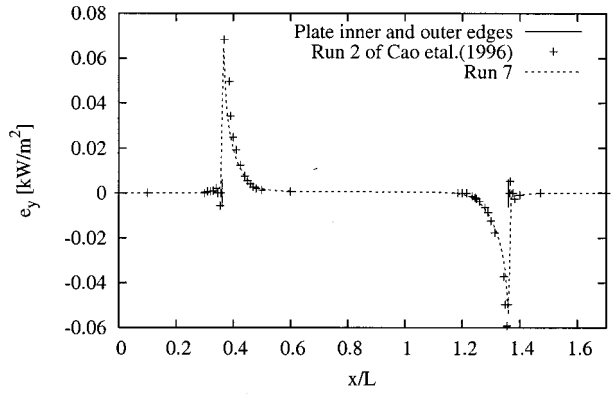

FIG. 3. Time-averaged energy flux density at the plate surface for run 2 of Cao *et al.* (1996) and run 7 of the current work.

VII. "LONG PLATE" SIMULATIONS

Figure 3 shows the energy flux at the plate surface for run 7 compared with run 2 of Cao *et al.* (1996). The time-averaged energy flux at the plate surface is positive for a heat flux leaving the domain through the plate and negative for it entering the domain. These sharp peaks in heat flux at the plate edges were also observed by Worlikar *et al.* (1998) numerically and by Mozurkewich (1998b) analytically.

In Fig. 4, the time-averaged energy flux distributions at the plate surface for various plate spacings are shown. Figure 4 shows that the width of the peak in the energy flux decreases as the plate spacing is reduced when $\delta_k/y_0 \geqslant 1.0$. The total energy flux leaving the outer edge of the plate and flowing through the gas and into the inner edge also reduces as the plate spacing is decreased. Figure 4 also shows some interesting trends with the plate spacing, especially at the outer plate edge, that were not identified previously.

The characteristic result in which energy flux leaves the outer edge of the plate and enters the inner edge changed to one in which energy flux entered each end of the plate at a plate spacing of $\delta_{km}/y_0 = 1.2$. The energy transfer is dis-

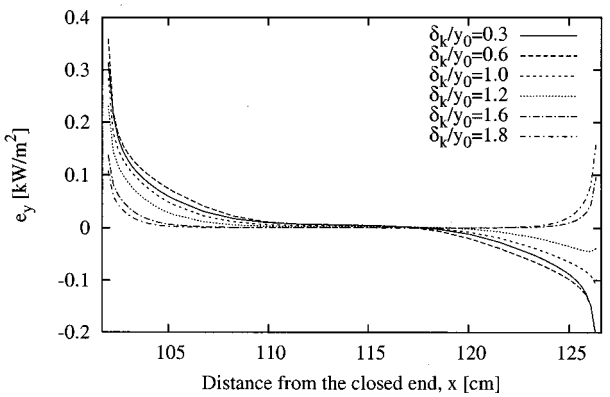

FIG. 4. Time-averaged energy flux entering the plate for different plate spacings (run 1; $\delta_k/y_0=0.3$, run 2; $\delta_k/y_0=0.6$, run 3; $\delta_k/y_0=1.0$, run 4; $\delta_k/y_0=1.2$, run 5; $\delta_k=1.6$, run 6; $\delta_k=1.8$).

played in terms of energy vectors in Figs. 5 and 6. Note that only the simulation domain near the plate is shown.

When $\delta_{km}/y_0=0.3$ (Fig. 5), the time-averaged energy vectors leaving the plate outer edge head towards BC_{os} near the plate surface and turn back towards the inner plate edge at approximately the thermal penetration distance from the plate ($\delta_{km}=0.24$ cm in Fig. 5). Energy vectors near the inner plate edge also start to point towards the plate edge at the thermal penetration depth away from the surface. When $\delta_{km}/y_0=1.2$ [Fig. 6(a)], the time-averaged energy vectors leaving the plate outer edge start to head towards the inner plate edge soon after they leave the outer edge. Energy vectors near the inner plate edge also head directly towards the plate. When $\delta_{km}/y_0=1.6$ [Fig. 6(b)], the energy vectors at both plate edges are directed towards the plate surface and there is no cycle-averaged net heat carried from the outer edge to the inner plate edge. This is attributed to increased energy dissipation as the plate spacing is reduced. This is further discussed later in this section.

Both Figs. 5 and 6 indicate a small amount of energy flux through the oscillatory boundary (to compensate for the energy dissipated in the simulation domain) which subsequently leaves the domain in the form of heat transferred to the plate. In fixing the oscillating variables at BC_{os} to be those of the 1D standing wave, the first two terms of Eq. (10)

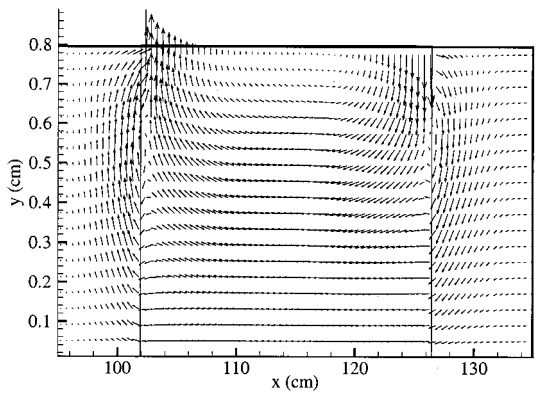

FIG. 5. Time-averaged energy vectors for $\delta_{km}/y_0=0.3$ (run 1), $M=0.03$.

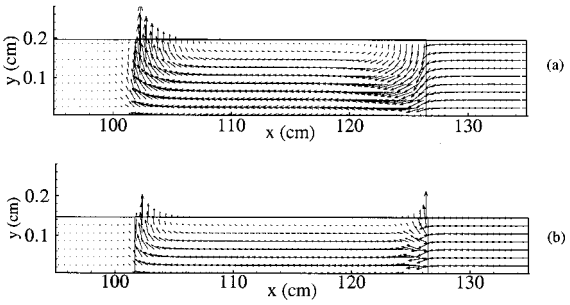

FIG. 6. Time-averaged energy vectors when (a) $\delta_{km}/y_0=1.2$ (run 4) and (b) $\delta_{km}/y_0=1.6$ (run 5). $M=0.03$.

and all but the fourth term of Eq. (11) are zero. Therefore, energy can only enter the domain through BC_{os} in the form of heat flux or flux due to internal friction. The magnitude of the total energy flux through this boundary is very small compared to the level of fluctuating energy flux within the domain (typically less than 1%). It is noted that specifying the boundary conditions in this way, which is quite different from how the conditions were specified in Cao *et al.*, resulted in good agreement between the two simulations (see Fig. 3).

For the simulation of thermoacoustic couples, an oscillating solid-wall boundary would be suitable. However, the boundary conditions used in the current work were chosen with an extension of the work to simulation of only the heat exchanger section in mind. In that case there will be an energy flux through the oscillating boundary.

The movement of the gas near the plate is shown by the paths taken by particles 1 to 9 for runs 1 and 5 in Figs. 7 and 8, respectively. x_E is the distance from the closed end of the tube, $x=0$, to the inner plate edge, point 3 in Fig. 2. The particle paths for run 4 were almost identical to those for run 5 and are not shown here. Particles 7, 8, and 9 in Figs. 7 and 8 start traveling just at the outer edge of the plate and the distance they travel in the x direction is approximately the particle displacement length.

There are some obvious differences in traces for particles at different locations in the domain. All particles, except 2 and 8, move mainly in the x direction with very little

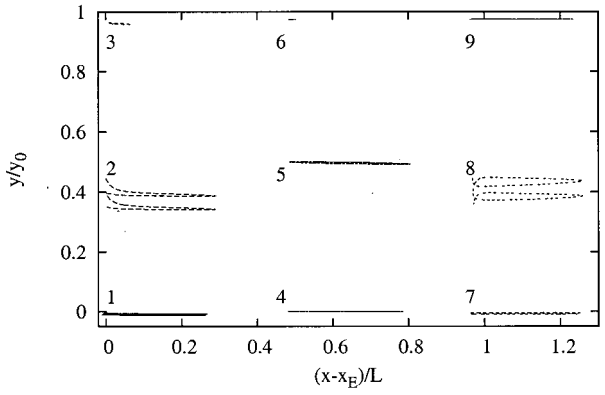

FIG. 7. Particle paths for nine particles when $\delta_{km}/y_0=0.3$ (run 1). $L=22u_1/\omega$.

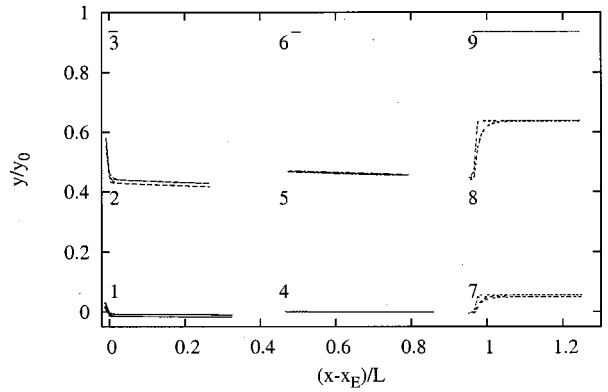

FIG. 8. Particle paths for nine particles when $\delta_{km}/y_0=1.6$ (run 5). $L=22u_1/\omega$.

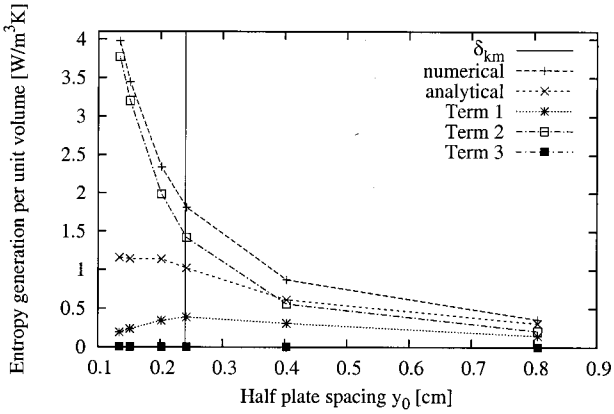

FIG. 9. Entropy generation rates for different plate spacings. (run 1; $y_0\simeq 0.81$ cm, run 2; $y_0\simeq 0.41$ cm, run 3; $y_0\simeq 0.24$ cm, run 4; $y_0\simeq 0.20$ cm, run 5; $y_0\simeq 0.15$ cm, run 6; $y_0\simeq 0.13$ cm).

y movement, although, for the smaller plate spacing, there is more *y* movement for particles 1 and 7. Particles 3 and 6, strongly influenced by viscous effects, move less than a quarter of the distance of the other particles for both test cases.

The largest differences are found in the movements of particles 2 and 8. When $\delta_{km}/y_0=1.6$, the particle traces show that particles 2 and 8 return to within less than $0.03y_0$ and $0.02y_0$, respectively of their starting positions. However, when $\delta_{km}/y_0=0.3$, the difference between the initial and the final positions is $0.05y_0$, and it is noted that y_0 is approximately five times that when $\delta_{km}/y_0=1.6$. Tests using two different time steps indicated that the difference between the starting and finishing points for particles 2 and 8 when $\delta_{km}/y_0=0.3$ is too great to be due to numerical errors in the tracking calculations.

This indicates that over a number of cycles, particles are moving away from the plate at these locations which must be compensated for by other particles replacing them from elsewhere in the domain. This is indicative of a larger scale, lower-frequency vortical motion just outside the plate edges.

This is similar to phenomena observed by Ozawa *et al.* (1999). Ozawa *et al.* visualized acoustic streaming in resonators with or without plates, at a drive ratio of 0.2%. Without plates, there are well-known large-scale vortices between the pressure node and antinode due to acoustic streaming. When Ozawa introduced a single plate or a multiple layer of plates spaced much wider apart than the thermal penetration depth, he observed a large vortex at either edge of the plates for both cases.

Ozawa's plate lengths were approximately 1/10th of the wavelength, which is of a similar order to the current ''long'' plates. It must be noted that the current work does not include the wall effect of the resonator in the simulation domain, yet the current simulation still indicated the possibility of vortical motion (of a scale set by the plate spacing) just outside both edges of the plate for smaller spacings.

In Fig. 9, the volume-averaged entropy generation rates versus plate spacing (runs 1 to 6) are shown, along with the analytically calculated entropy generation rates at the plate surface. (The vertical line in the figure indicates the magnitude of the thermal penetration depth.) To calculate the volume-averaged entropy generation, Eq. (14) was evaluated at each cell, multiplied by the cell volume, and summed over the whole domain. The sum was then divided by the domain volume. The analytical curve is generated from Eq. (15), which represents the energy dissipation at the plate surface, divided by the mean temperature and the domain volume.

In order to investigate what physical mechanisms contribute to entropy generation, terms in Eq. (14) are grouped and labeled as follows:

(i) Term 1: $(K/T^2)(\partial T/\partial y)^2$, entropy generation due to the dominant gradient in temperature.
(ii) Term 2: $(\mu/T)(\partial u/\partial y)^2$, entropy generation due to the dominant viscous effects.
(iii) Term 3: The remainder of the terms in Eq. (14).

These terms are plotted in Figs. 9 and 10.

The analytically calculated entropy generation rates agree with the numerical results at larger plate spacings, but not for smaller spacings. This is reasonable because the analytical expression was derived based on the assumption that $y_0 \gg \delta_{km}$. Note that the entropy generation is much higher than that predicted analytically for the smaller plate spacings. For all test cases, the difference between the entropy generation calculated over the whole domain and that in the plate

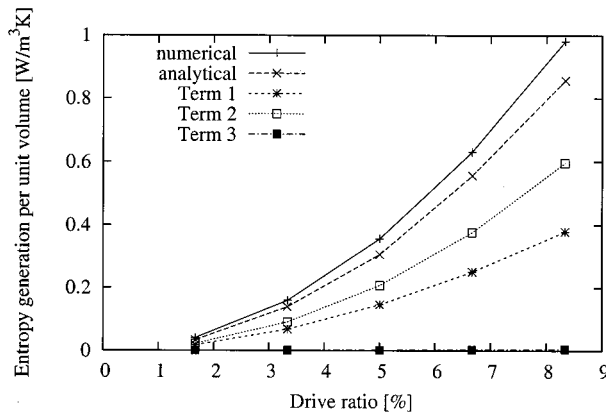

FIG. 10. Entropy generation for different drive ratios. $\delta_{km}/y_0=0.3$. (run 7; drive ratio$\simeq$1.7%, run 8; 3.4%, run 1; 5.1%, run 9; 6.8%, run 10; 8.5%).

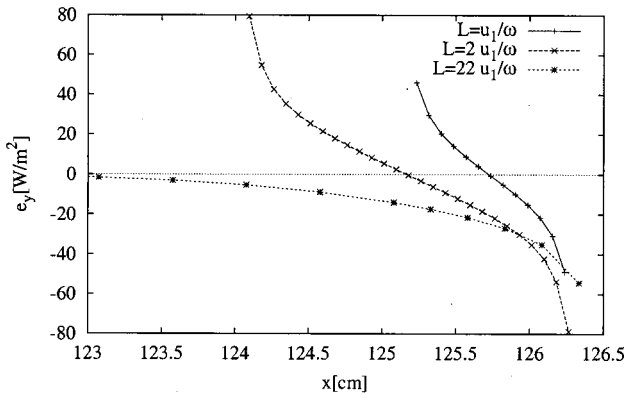

FIG. 11. Time-averaged energy flux density (y component) at the outer edge of the plate for three different plate lengths (run 14; $L=u_1/\omega$, run 11; $L=2u_1/\omega$, and run 7; $L=22u_1/\omega$). $y_0=3.3\delta_{km}$, $2u_1/\omega=2.3$ cm. The outer edges of all plates are at $x\simeq 126.2$ cm. The inner edges of the plates are at $x\simeq 124.2$, 125.2, and 101.2 cm, respectively.

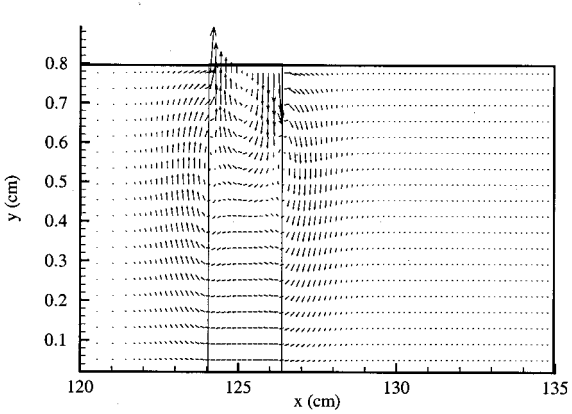

FIG. 12. Time-averaged energy vectors for run 11.

section was less than 1%. Thus, as would be expected, it is only in the vicinity of the plate that significant entropy generation occurs.

Figure 9 also shows that the dominant parameters leading to entropy generation are y gradients of temperature and y gradients in the x component of velocity (terms 1 and 2), respectively. The entropy generated due to temperature gradients in the y direction increases as the plate spacing increases. Note that this term decreases as y_0 increases beyond 0.24 cm. Although the total entropy generation in the simulation domain continues to increase as y_0 increase, term 1 (which is a per-unit volume term) does decrease. This indicates that the rate of increase in term 1 drops when the plate spacing is larger than twice the thermal penetration depth. This can be explained by the fact that the temperature gradient is large only within the thermal boundary layer. Term 2, the entropy generation due to dominant viscous effects, increases quadratically as the plate spacing is reduced.

As the plate spacing is reduced, the amount of heat pumped from one end of the plate to the other decreases (see Fig. 4). However, also as the plate spacing reduces, energy dissipation near the plate increases (see Fig. 9) and the highest rates of energy dissipation occur at the ends of the plates. The phenomenon of heat entering the plate at both ends for small plate spacings is attributed to a balance between these two effects.

The entropy generation over the whole simulation domain versus the drive ratio (or Mach number) is shown in Fig. 10 using the simulation results of runs 1 and 7 to 10 when $y_0=3\delta_{km}$. The figure also shows terms 1 to 3 of Eq. (14). The quadratic dependence was expected from the fact that the dominant terms in Eq. (14) vary with the square of temperature and velocity. The analytically calculated energy dissipation at the plate surface and the numerically calculated entropy generation over the whole domain agree at all drive ratios to within approximately 10%. This shows that most dissipation occurs at the plate surface for this plate spacing and for all drive ratios tested. Again, terms 1 and 2 are dominant and the magnitudes of each increase as the drive ratio increases.

VIII. "SHORT PLATE" SIMULATIONS

The time-averaged heat flux at the plate surface, $\dot{e}_y$, is plotted in Fig. 11 for plate lengths of $2u_1/\omega$ and u_1/ω when $y_0=3.3\delta_{km}$. The corresponding energy flux vectors are shown in Figs. 12 and 13. The long plate (run 7) result is also shown in Fig. 11 but only results at the outer end of the plate are shown. The results show that the heat transfer is in opposite directions at the inner and outer plate edges. This indicates that heat is pumped from the outer to the inner edge of the plate. This is in qualitative agreement with results of Worlikar and Knio (1999). The shapes of the curves in Fig. 11 are very similar to those for the long plates, except that for the short plates there is no flat region (where $\dot{e}_y$ is near zero).

Figure 11 shows that the distance from the plate edge where significant heat transfer occurs is approximately the particle displacement distance. For the operating conditions tested, this suggests that when the plate is more than four times longer than the particle displacement distance, the net amount of heat transfer from one end of the plate to the other is equal if the plate spacings are the same.

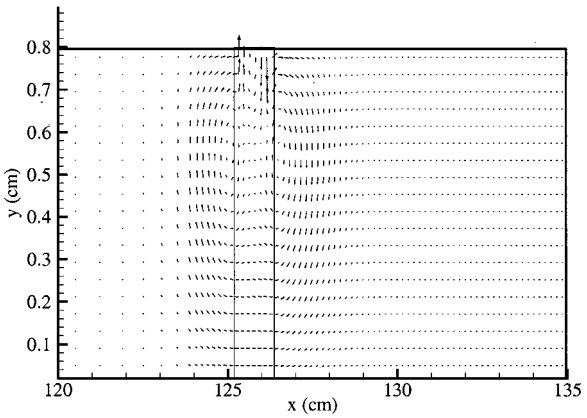

FIG. 13. Time-averaged energy vectors for run 14.

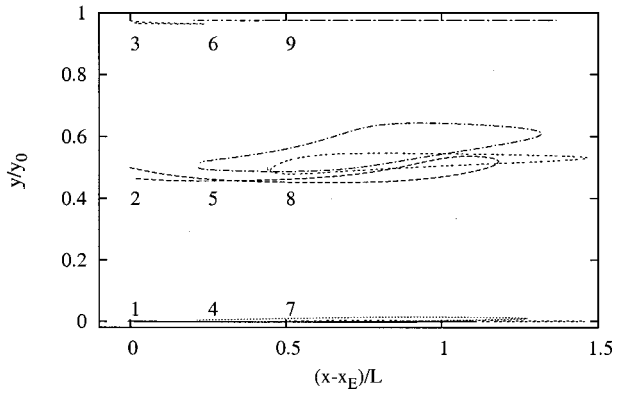

FIG. 14. Particle paths for nine particles for run 11 where $L=2u_1/\omega$.

The particle traces for run 11 are shown in Fig. 14. The results for run 14 were almost identical to those for run 11. The particle displacements are the same as the plate length in Fig. 14. These are in good agreement with the preliminary estimates of particle displacement distance which were calculated for ideal standing waves at the same location. The figures also show that particles 2, 5, and 8 (those at a quarter of the interplate spacing) have a large y movement resulting in looped paths. The maximum difference between the initial and the final locations are approximately 2% of the y-domain length and, given the accuracy of the particle traces, the fact that particles 2, 5, and 8 of Fig. 14 do not return to their original positions is again an indication of a possible vortical motion outside the plate edge.

The time-averaged heat flux to the plates, presented in Fig. 15 when $y_0=3\delta_{km}$, shows that a heat-pumping effect exists at the plate surface even though the plate spacing is equal to the thermal penetration depth. However, when the plate spacing is further reduced to $y_0=\delta_{km}/3$, the energy dissipation is dominant and the heat-pumping effects are no longer seen. The energy vector pattern for $y_0=\delta_{km}/2$ is similar to that for $y_0=3\delta_{km}$. However, the pattern changes significantly at smaller plate spacings. The energy vectors when

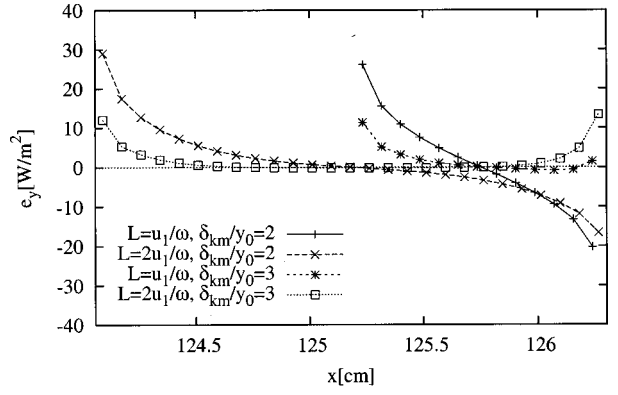

FIG. 15. Time-averaged energy flux density in the y direction at the surface of the short plates when $\delta_{km}/y_0=2$ (run 15; $L=u_1/\omega$, run 12; $L=2u_1/\omega$) and $\delta_{km}/y_0=3$ (run 16; $L=u_1/\omega$, run 13; $L=2u_1/\omega$). The outer edges of all plates are at $x\simeq 126.2$ cm. The inner edges of the plates are at $x\simeq 125.2$ and 124.2 cm, respectively.

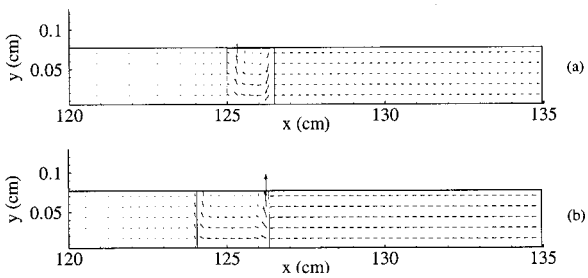

FIG. 16. Time-averaged energy vectors when $\delta_{km}/y_0=3$ for (a) run 16 where $L=u_1/\omega$; (b) run 13 where $L=2u_1/\omega$.

$y_0=\delta_{km}/3$ for $L=u_1/\omega$ and $L=2u_1/\omega$ are presented in Figs. 16(a) and (b).

The particle traces for the cases when $y_0=\delta_{km}/2$ are almost identical to those in Fig. 14, but the characteristic shapes of the particle traces change when $y_0=\delta_{km}/3$, as shown in Fig. 17. Traces for particles 2, 5, and 8 have y displacements but there are no loops in their tracks.

IX. CONCLUSION

The simulation results show that a heat-pumping effect can be seen, not only on the long plates but also on the shortest plates tested, when plate spacings are greater than the thermal penetration depth. As the plate spacing approaches the thermal penetration depth, energy dissipation near the plate increases quadratically and no heat-pumping effect is observed. The energy dissipation increases quadratically with Mach number.

The time-averaged heat transfer to and from the plates is concentrated at the edges of the plates for all test cases. At constant Mach number, the width of the region where there is substantial heat transfer decreases as the plate spacing is reduced.

Particle traces for the test case with the largest plate spacing and a long plate show evidence of vortical motion outside both edges of the plate. The short plate simulations also indicate this vortical motion outside the plates. In addition, particle traces indicate that the gas between the plate surface and the symmetrical boundary prescribes a path with

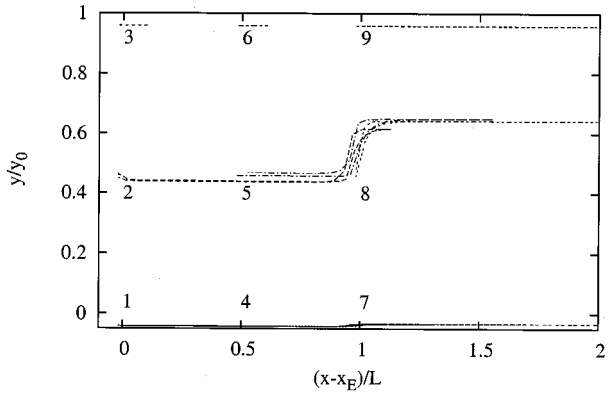

FIG. 17. Particle paths for nine particles for run 13 where $L=2u_1/\omega$, $\delta_{km}/y_0=3$.

a loop in it. However, to confirm the presence of vortical motion outside the plates (especially for the short plate), more particles should be traced, and visualization experiments are required. As the plate spacing is reduced, evidence for vortical motion diminishes.

A number of suggestions for the design of regenerators and heat exchangers can be drawn from these simulation results. The results show that, in terms of the total amount of heat pumped, it is not necessary to have plates longer than four times the particle displacement distance. Any extra surface area contributes to energy dissipation. However, when a certain temperature difference is required along the plate, as is the case of the regenerator plate, short plates will result in large temperature gradients along the plate, in which case there will be heat conduction losses along the plate.

For the design of heat exchangers, plate spacings of the order of the thermal penetration depth may not be appropriate, since the energy dissipation increases with the inverse square of the plate spacing. Therefore, plate spacing should be determined carefully using second law analysis to minimize the entropy generation (Ishikawa and Hobson, 1996).

ACKNOWLEDGMENTS

The authors are grateful for discussions with Professor. M. Ozawa and Dr. A. Tominaga, and suggestions from Dr. G. Swift.

Bejan, A. (**1982**). *Entropy Generation Through Heat and Fluid Flow* (Wiley, New York).

Bird, R. B., Stewart, W. E., and Lightfoot, E. N. (**1960**). *Transport Phenomena* (Wiley, New York).

Cao, N., Olson, J. R., Swift, G. W., and Chen, S. (**1996**). ''Energy flux density in a thermoacoustic couple,'' J. Acoust. Soc. Am. **99**, 3456–3464.

Chapman, S., and Cowling, T. G. (**1970**). *The Mathematical Theory of Non-uniform Gases*, 3rd ed. (Cambridge University Press, London).

Ishikawa, H. (**2000**). ''Investigations of optimum design of heat exchangers of thermoacoustic engines,'' Ph.D. thesis, The University of Queensland. Available at http://adt.caul.edu.au

Ishikawa, H., and Hobson, P. A. (**1996**). ''Optimization of heat exchanger design in a thermoacoustic engine using a second law analysis,'' Int. Commun. Heat Mass Transfer **23**(3), 325–334.

Landau, L. D., and Lifshitz, E. M. (**1959**). *Fluid Mechanics* (Pergamon, London).

Merkli, P., and Thomann, H. (**1975**). ''Transition to turbulence in oscillating pipe flow,'' J. Fluid Mech. **68**, 567–575.

Mozurkewich, G. (**1998a**). ''A model for transverse heat transfer in thermoacoustics,'' J. Acoust. Soc. Am. **103**, 3318–3326.

Mozurkewich, G. (**1998b**). ''Time-average temperature distribution in a thermoacoustic stack,'' J. Acoust. Soc. Am. **103**, 380–388.

Ozawa, M., Kunihiro, K., and Kawamoto, A. (**1999**). ''Flow visualization of acoustic streaming in a resonance tube refrigerator,'' in Technology Reports of Kansai University, March, (41):35–44.

Patankar, S. V., and Spalding, D. B. (**1972**). ''A calculation procedure for heat, mass and momentum transfer in three-dimensional parabolic flows,'' Int. J. Heat Mass Transf. **15**, 1787–1806.

Spalding, D. B. (**1981**). ''Mathematical modelling of fluid-mechanics, heat-transfer, and chemical-reaction processes. A lecture course,'' CFDU Report HTS 180/1, Imperial College, London.

Spalding, D. B. (**1991**). *The* PHOENICS *Beginner's Guide TR100*, CHAM, Bakery House, 40 High Street, Wimbledon Village, London SW19 5AU, UK.

Swift, G. W. (**1988**). ''Thermoacoustic engines,'' J. Acoust. Soc. Am. **84**, 1145–1180.

Swift, G. W. (**1999**). ''Thermoacoustics: A unifying perspective for some engines and refrigerators,'' Los Alamos. Available at http://www.lanl.gov/projects/thermoacoustics/Book/index.html

Watanabe, M., Prosperetti, A., and Yuan, H. (**1997**). ''A simplified model for linear and nonlinear processes in thermoacoustic prime movers. I. Model and linear theory,'' J. Acoust. Soc. Am. **102**, 3484–3496.

Wheatley, J., Hofler, T., Swift, G. W., and Migliori, A. (**1983**). ''Experiments with an intrinsically irreversible acoustic heat engine,'' Phys. Rev. Lett. **50**(7), 499–502.

Worlikar, A. S., and Knio, O. M. (**1996**). ''Numerical modeling of thermoacoustic refrigerator. I. Unsteady flow around the stack,'' J. Comput. Phys. **127**(5), 424–451.

Worlikar, A. S., and Knio, O. M. (**1999**). ''Numerical study of oscillatory flow and heat transfer in a loaded thermoacoustic stack,'' Numer. Heat Transfer, Part A **35**, 49–65.

Worlikar, A. S., Knio, O. M., and Klein, R. (**1998**). ''Numerical modeling of thermoacoustic refrigerator. II. Stratified flow around the stack,'' J. Comput. Phys. **144**, 299–324.

Yuan, H., Karpov, S., and Prosperetti, A. (**1997**). ''A simplified model for linear and nonlinear processes in thermoacoustic prime movers. I. Nonlinear oscillations,'' J. Acoust. Soc. Am. **102**, 3497–3506.